Front. Struct. Civ. Eng. 2023, 17(4): 546–565
https://doi.org/10.1007/s11709-023-0943-4

RESEARCH ARTICLE

Numerical modeling of current-induced scour around multi-wall foundation using large-eddy simulation

Jiujiang WU[a,b*], Lingjuan WANG[c], Qiangong CHENG[d]

[a] *Shock and Vibration of Engineering Materials and Structures Key Laboratory of Sichuan Province, Southwest University of Science and Technology, Mianyang 621010, China*

[b] *Department of Civil and Environmental Engineering, Western University, London, ON N6A 5B9, Canada*

[c] *Office of International Students Education, Southwest University of Science and Technology, Mianyang 621010, China*

[d] *Faculty of Geosciences and Environmental Engineering, Southwest Jiaotong University, Chengdu 610031, China*

[*] *Corresponding author. E-mail: wujiujiang1988@126.com*

ABSTRACT Scouring is one of the primary triggers of failure for bridges across rivers or seas. However, research concerning the scour mechanism of multi-wall foundations (MWFs) remains scarce, hindering the further application of MWFs. In this study, for the first time, the scouring effect caused by unidirectional flow around MWFs was examined numerically using FLOW-3D involving a large-eddy simulation. Initially, the applicability of the scouring model and input parameters was validated using a case study based on published measured data. Subsequently, the scouring effects of four MWFs with different wall arrangements and inflow angles, including the flow field analysis and scour pit and depth, were investigated thoroughly. It was found that the maximum scour depth of MWFs with an inflow angle of 0° was smaller than that of those with an inflow angle of 45°, regardless of the wall arrangement. Meanwhile, changing the inflow angle significantly affects the scour characteristics of MWFs arranged in parallel. In practical engineering, MWFs arranged in parallel are preferred considering the need for scouring resistance. However, a comparative analysis should be performed to consider comprehensively whether to adopt the form of a round wall arrangement when the inflow angle is not 0° or the inflow direction is changeable.

KEYWORDS multi-wall foundation, current-induced scour, bridge foundation, large-eddy simulation, numerical analysis

1 Introduction

Owing to their good seismic performance, their large bearing capacity, and the characteristics of low construction disturbance and noise to adjacent buildings, diaphragm walls have been widely used as bridge foundations to support the loads transferred from the superstructure and resist the lateral loads generated by waves and currents. A multi-wall foundation (MWF) is a new type of diaphragm wall that has been applied as a bridge foundation in many practical projects in Japan. The first application of the MWF technique was a nine-span continuous girder bridge constructed at Tsurumi District, Yokohama City, Japan, on the Prefectural Highway Coastline [1].

The main feature of the MWF is that it exhibits different bearing characteristics and deformation properties along and across the bridge axis. Meanwhile, a reasonable design solution can be developed for an MWF with an allowable bearing capacity and deformation value by changing the shape, arrangement, and number of wall segments. Because the maximum length of each wall segment is less than 10 m [1], it is unnecessary to consider the setting of the joint, which can be a structural weakness of other standard diaphragm wall foundations. Therefore, a higher construction efficiency can be achieved for MWFs than for traditional diaphragm wall bridge foundations, such as lattice-shaped diaphragm walls [2]. In addition, the cross-sectional cap area of the MWF is significantly reduced compared with that of a pile group foundation [3], which can reduce the construction area accordingly.

Article history: Received Aug 13, 2022; Accepted Nov 19, 2022

Scour is a natural phenomenon in which the action of water causes river or seabed erosion. Its occurrence and development result from the interaction between water currents/waves, bridge foundations, and river/seabed materials. Sutherland [4] found that 29 of 108 bridges damaged in New Zealand were affected by scour. Wardhana and Hadipriono [5] investigated more than 500 bridge failures between 1989 and 2000 and found that more than half of the damage was water related. Therefore, scour is a primary failure trigger for bridges across rivers or seas. Accordingly, many numerical studies have been conducted to determine the scouring process around bridge piers. For instance, Najafzadeh and Barani [6] introduced a new application for predicting the scour depth around a vertical pier using genetic programming and a backpropagation algorithm. Subsequently, more-reliable prediction methods have been developed involving neuro-fuzzy, artificial intelligence, and other techniques [7–11].

Currently, the use of complex piers to build bridges has become widespread, and many scouring investigations around bridge piers with complex foundations have been conducted accordingly [12]. Liang et al. [13] presented an analytical model to investigate the extreme scour effect on the buckling of bridge piles in soft clay by considering the stress history of the remaining soils. Amini and Parto [14] conducted a numerical simulation of the flow field around twin piles using FLOW-3D. The results of the flow field simulation showed that the Reynolds number and pile spacing were the most-influential variables in the formation of vortices. To address the effects of uniform and non-uniform pile spacing on the equilibrium scour depth, Amini and Solaimani [15] conducted laboratory experiments under steady clear-water conditions. Hosseini et al. [16] used a bagged neural network to estimate the scour depth around pile groups, and their analysis showed that the pile diameter and spacing are dominant contributors. Khaledi et al. [17] simulated the scour width and length variations around complex piers under clear-water conditions. It was found that the variation in scour hole dimensions could be categorized into two cases: before and after pile cap undercutting.

As described previously, the MWF is a novel type of bridge foundation. Relevant research concerning the scour mechanism of MWFs remains scarce, which can hinder further application of MWFs. The purpose of this study was to investigate the scouring effect caused by unidirectional flow around MWFs. Initially, the applicability of the scouring model and input parameters was validated using a case study based on published measured data. Subsequently, the scouring effects for four MWFs with different wall arrangements and inflow angles, including the flow field analysis and scour pit and depth, were investigated thoroughly. The results of this study can be used by engineers and bridge designers to improve the safety of bridge piers adopting MWFs in terms of scouring by determining the wall arrangement and inflow angle.

2 Structural and wall arrangement regulation of a multi-wall foundation

The MWF is a new type of diaphragm wall consisting of wall segments arranged in a specific pattern. The wall segments are connected to a cap by rigid connectors to form a rigid foundation, as shown in Fig. 1. The wall segments can be arranged in parallel (Fig. 1(b)) or in a "round" configuration (Fig. 1(c)). At the beginning of the development of the MWF foundation, the wall layout is generally designed to be set in parallel, but, considering the impact of earthquakes, the horizontal stiffness must

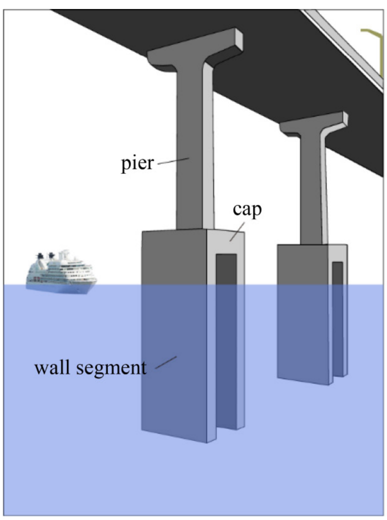

(a)

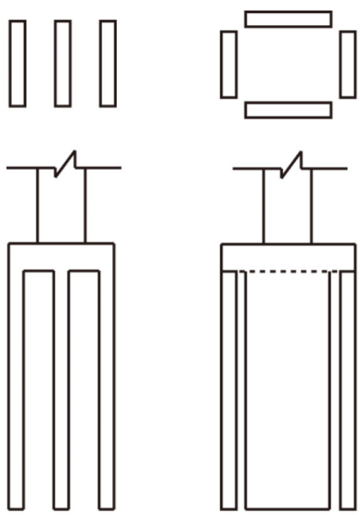

(b) (c)

Fig. 1 Demonstration of MWF: (a) general view; (b) parallel wall arrangement; (c) round wall arrangement.

be increased in some usage scenarios; therefore, the round wall arrangement is used, as shown in Fig. 1(c).

3 Mathematical model and basic theory

The Navier−Stokes (N−S) equation is used as the governing equation of the water flow, and the turbulence simulation is based on the theory of large-eddy simulation (LES) [18]. The sediment motion equation includes the suspended-load diffusion and sediment transport equations. The description and visualization of the sediment bed uses fractional area/volume obstacle representation (FAVOR) technology [19].

3.1 Governing equations of water flow

The continuity equation can be defined as

$$\frac{\partial(uA_x)}{\partial x}+\frac{\partial(vA_y)}{\partial y}+\frac{\partial(wA_z)}{\partial z}=0. \tag{1}$$

The momentum equation of the water flow is given as

$$\frac{\partial u}{\partial t}+\frac{1}{V_{\mathrm{F}}}\left(uA_x\frac{\partial u}{\partial x}+vA_y\frac{\partial u}{\partial y}+wA_z\frac{\partial u}{\partial z}\right)=-\frac{1}{\rho}\frac{\partial p}{\partial x}+G_x+f_x, \tag{2}$$

$$\frac{\partial v}{\partial t}+\frac{1}{V_{\mathrm{F}}}\left(uA_x\frac{\partial v}{\partial x}+vA_y\frac{\partial v}{\partial y}+wA_z\frac{\partial v}{\partial z}\right)=-\frac{1}{\rho}\frac{\partial p}{\partial y}+G_y+f_y, \tag{3}$$

$$\frac{\partial w}{\partial t}+\frac{1}{V_{\mathrm{F}}}\left(uA_x\frac{\partial w}{\partial x}+vA_y\frac{\partial w}{\partial y}+wA_z\frac{\partial w}{\partial z}\right)=-\frac{1}{\rho}\frac{\partial p}{\partial z}+G_z+f_z, \tag{4}$$

where u, v, and w are the velocity components in the x-, y-, and z-axis directions, G_x, G_y, and G_z are the body accelerations in the x-, y-, and z-axis directions, f_x, f_y, and f_z are the accelerations of the viscous force in the x-, y-, and z-axis directions, A_x, A_y, and A_z are the fluid area fractions in the x-, y-, and z-axis directions, V_{F} is the fluid volume fraction, ρ is the fluid density, and p is the pressure acting on the fluid element.

3.2 Large-eddy simulation governing equations

Compared with the commonly used turbulence models, such as the renormalization group and k–ε model [20,21], the basic idea of LES is to decompose the instantaneous pulsating motion in turbulent flow into two parts, large scale and small scale, by the filtering method. The large-scale turbulent flow vortices are simulated by solving the momentum and continuity equations, and the effects of small-scale eddies are represented by a sub-grid model. After filtering the incompressible N−S equation, the governing equations of the LES can be obtained as

$$\frac{\partial\rho}{\partial t}+\frac{\partial}{\partial x_i}(\rho\bar{u}_i)=0, \tag{5}$$

$$\rho\frac{\partial\bar{u}_i}{\partial t}+\rho\frac{\partial}{\partial x_j}(\bar{u}_i\bar{u}_j)=-\frac{\partial\bar{p}}{\partial x_i}+\mu\frac{\partial^2\bar{u}_i}{\partial x_i\partial x_j}-\rho\frac{\partial\tau_{ij}}{\partial x_j}, \tag{6}$$

$$\tau_{ij}=\overline{u_iu_j}-\bar{u}_i\bar{u}_j, \tag{7}$$

where u_i and u_j are the filtered velocity components of the flow field, μ is the fluid viscosity coefficient, and τ_{ij} is the stress tensor, which can be defined based on the Smagorinsky−Lilly subgrid model [22]:

$$\tau_{ij}=-2v_{\mathrm{t}}\bar{S}_{ij}+\frac{\tau_{\mathrm{kk}}\delta_{ij}}{3}, \tag{8}$$

where τ_{kk} is the subgrid turbulent kinetic energy, v_{t} is the eddy viscosity coefficient, and $\bar{S}_{ij}$ is the filtered velocity deformation tensor, which can be defined as

$$\bar{S}_{ij}=\frac{1}{2}\left(\frac{\partial\bar{u}_i}{\partial x_j}+\frac{\partial\bar{u}_j}{\partial x_i}\right). \tag{9}$$

3.3 Calculation of riverbed/seabed deformation

3.3.1 Critical shields parameter

The critical shear stress is used as the condition to judge the initiation of sediment, and the Soulsby–Whitehouse formula [23] is used to calculate the dimensionless Shields coefficient of θ_{cr}. The curve calculated using this formula fits well with the Shields curve and is widely used [24]. When the local Shields coefficient θ_{i} is greater than the critical Shields coefficient θ_{cr}, sand is initiated on the riverbed/seabed surface.

$$\theta_{\mathrm{cr}}=\frac{0.3}{1+1.2d_*}+0.055[1-\exp(-0.02d_*)], \tag{10}$$

where $d_*=d_{50}\left[\frac{\rho(\rho_{\mathrm{s}}-\rho)g}{\mu^2}\right]^{1/3}$, ρ_{s} is the density of the sediment, d_{50} is the median size of the sediment, which is 0.385 mm, g is the gravity acceleration.

Considering the influence of the slope on the critical initiation of sediment particles, Soulsby [23] revised Eq. (7) as

$$\theta'_{\mathrm{cr}}=\theta_{\mathrm{cr}}\frac{\cos\psi\sin\lambda+\sqrt{\cos^2\lambda\tan^2\varphi-\sin^2\psi\sin^2\lambda}}{\tan\varphi}, \tag{11}$$

where λ is the slope of the riverbed/seabed, φ is the response angle of the sediment, and ψ is the angle between the direction of water flow and the uphill direction.

3.3.2 Entrainment and sedimentation

The calculation model of entrainment and sedimentation is based on the theory of Mastbergen and van Den Berg [25]. Zhang et al. [26] adopted this model to simulate numerically the local scour around three cylinders with different arrangements, and they obtained a relatively satisfactory result. The lifting speed of the sediment carried by the water flow u_{lift} can be obtained by Ref. [25]:

$$u_{\mathrm{lift}} = \alpha_{\mathrm{i}} n_{\mathrm{s}} d_*^{0.3} (\theta_{\mathrm{i}} - \theta'_{\mathrm{cr}})^{1.5} \sqrt{\frac{d_{50}(\rho_{\mathrm{s}} - \rho) g}{\rho}}, \tag{12}$$

where $\theta_{\mathrm{i}} = \dfrac{\tau}{d_{50}(\rho_{\mathrm{s}} - \rho) g}$, τ is the local shear stress, α_{i} is the entrainment coefficient (0.018), and n_{s} is the normal vector of the packed bed surface.

The settling velocity of the packed bed u_{settle} is calculated using the sedimentation velocity formula proposed by Soulsby [23] as

$$u_{\mathrm{settle}} = \frac{\mu}{d_{50}} [(10.36^2 + 1.049 d_*^3)^{0.5} - 10.36]. \tag{13}$$

3.3.3 Bedload transportation

The rolling or jumping of sediment particles on a packed bed surface is the basic form of bedload transportation and can be calculated using van Rijn's formula for the bedload transport rate [27]. The single-width bedload transport rate of the surface sediment on the packed bed surface q_{b} is defined as

$$q_{\mathrm{b}} = \Phi \left[g d^3 \left(\frac{\rho_{\mathrm{s}} - \rho}{\rho} \right) d^3 \right]^{0.5}, \tag{14}$$

where $\Phi = \beta d_*^{-0.3} \left(\dfrac{\theta_{\mathrm{i}}}{\theta_{\mathrm{cr}}} - 1.0 \right)^{2.1}$, and β is the bedload coefficient (0.053).

The bedload layer thickness δ is estimated using the formula of van Rijn [27]:

$$\delta = d[0.3 d_*^{0.7} (\frac{\theta_{\mathrm{i}}}{\theta_{\mathrm{cr}}} - 1)^{0.5}]. \tag{15}$$

3.3.4 Description of the seabed/riverbed deformation

FAVOR technology in FLOW-3D uses the solid volume fraction in each grid to determine the solid surface. It can define independent and complex geometries inside a structured grid to use simple rectangular grids to represent an arbitrarily complex geometry. In the fluid area, the sand content rate in each grid is calculated using Eqs. (10)–(15). A settlement appears when the sand content rate is greater than the maximum sand content rate. FAVOR technology is used in the bedload transport model to describe the shape of the packed bed accurately by calculating the area and volume fraction parameters of the sediment in each grid during the entire scouring process.

4 Numerical modeling and parameter input

4.1 Validation of the scouring model

The experiment conducted by Roulund et al. [28] concerning a cylindrical pile is widely used in studies involving nontraditional pile foundations, such as the umbrella suction anchor foundation [29] and tree root foundation [30], to validate their numerical scouring model and parameters. To verify the reliability of the scour model adopted in this study, the data measured by Roulund et al. [28] are used.

The numerical validation model, based on the test setup of the scour experiment by Roulund et al. [28], is illustrated in Fig. 2. The total length and width of the computing domain are 20D and 9D (D is the diameter of the pile), respectively. The cylindrical monopile is located in the upper part of the computational domain, and its center is 6D from the inlet boundary and 14D from the outlet boundary. The mesh has 295107 nonuniform cells, and the cells are set to a finer size close to the cylindrical monopile. A velocity profile obtained from the simulation of turbulent flow over a flat plate was used at the inlet boundary of the mesh block. The initial time step of the numerical verification model is 0.001 s, the minimum time step is 1×10^{-12} s, and the total simulation time is 6000 s. The detailed numerical parameters are listed in Table 1.

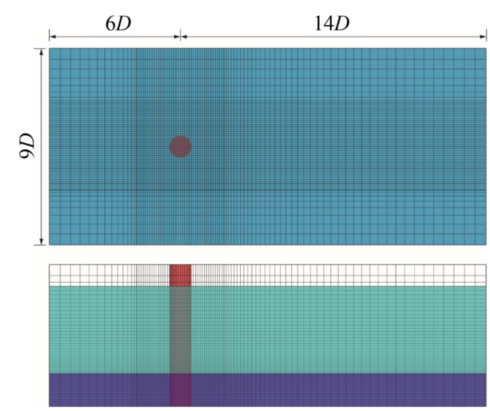

Fig. 2 Computing domain and mesh.

Figure 3 shows a simulation of the development process of the local scour pit. The shape and development of the simulated scour pit are roughly consistent with the results observed in the laboratory test conducted by Roulund et al. [28]. Figures 4 and 5 show the local scour depth development at the upstream and downstream edges of the pile, respectively. The numerical results agree well with the data measured by Roulund et al. [28]. Local scour develops around the pile body, and the maximum value appears in the inlet direction immediately before the pile.

The comparative analysis of the simulation and test results reveals that, regardless of the maximum scour depth of the local scour pits or the distribution shape of the scour pits, the simulation and test results agree quite well. The simulation has high precision, and the obtained calculation results are reliable.

Table 1 Parameter setup of the numerical validation model

parameter	value
pile diameter (cm)	10
water velocity (cm/s)	46
water depth (cm)	40
sediment diameter (cm)	0.026
sediment density (kg/m^3)	2650
critical shield number	0.05
entrainment coefficient	0.018
bedload coefficient	8
angle of response (°)	32

4.2 Computational domain and modeling of MWF

Figure 6 shows the setup of the numerical model for the simulation of an MWF subjected to current-induced scouring, where the computational domain and parameters refer to the pile case setup described in Subsection 3.1. Specifically, the 3D computational domain is 9.00 m long, 5.05 m wide, and 1.00 m high, including 0.40 m of the packed sediment bed and 0.40 m of fluid. Figure 6 illustrates the boundary condition in the scour model establishment, which sets the grid overlay boundary at the inlet, outflow at the outlet, top with specified pressure, right and left sides with symmetry, and bottom with the wall. At the inlet boundary of the mesh block, the grid overlay boundary technique was set to enable a velocity profile to be obtained from a simulation of turbulent flow over a flat plate, which can simulate the actual condition of the flow velocity field. The symmetry boundary condition is set to the right and left sides to reduce the influence of the flow turbulence from both sides. In addition, the top is set with a specified pressure boundary to simulate the air boundary at one-standard-atmosphere pressure.

In simulating the coupled motion of water flow and sediment, mesh accuracy and quantity are the most important factors affecting the numerical simulation results and computational efficiency. To capture the detailed characteristics of the sand bed around the cylinder accurately, the meshing must be sufficiently accurate, which usually leads to the multiplication of the number of meshes and a rapid increase in the calculation amount, which seriously affects the calculation

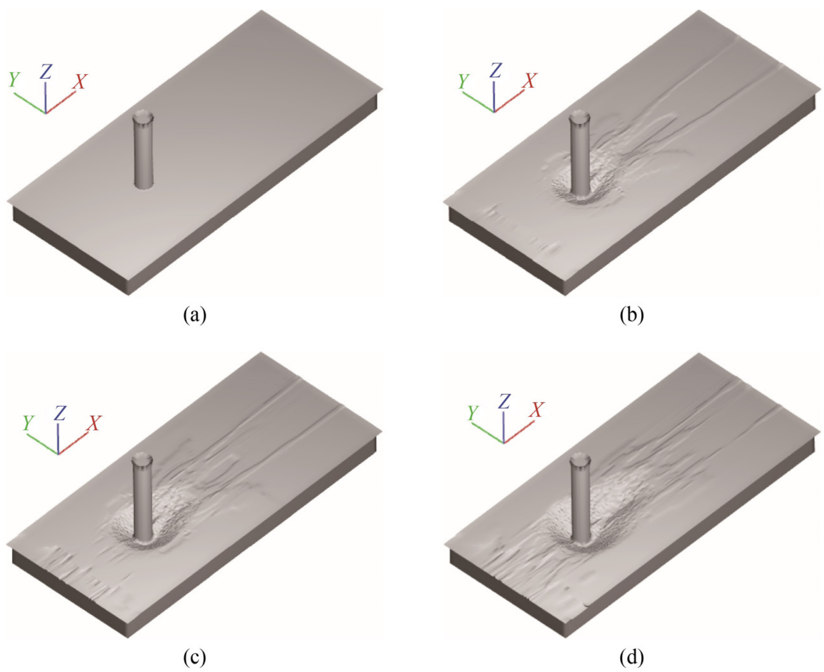

Fig. 3 Local scour pit development: (a) 0 min; (b) 5 min; (c) 20 min, and (d) 60 min.

efficiency. To reduce the computational effort, a nested mesh technique was applied to discretize the computational domain with a global cell size of 0.1 m in which the extent of the local refinement around the MWF is 1.8 m × 1.8 m, and the size of the local grid is 0.03 m, as illustrated in Fig. 6. In addition, the mesh near the sand bed is refined using the same principle. The total number of cells in the grids is approximately 0.4 million for each MWF model, reducing the number of units and ensuring the accuracy of the calculation.

To investigate the influence of the wall arrangement and current direction on the scour situation of MWFs, four MWF models were adopted in this study. Specifically, two MWFs with parallel-arranged walls (α = 0° and 45°, where α is the angle between the current direction and the longitudinal bridge direction, as shown in Fig. 7) and two MWFs with round-arranged walls (α = 0° and 45°) were investigated in the scour simulation under the setup shown in Fig. 7. The sedimentation and scour model was used with a specified sediment diameter and density (listed in Table 1), and all other settings refer to the corresponding sections described previously. The value of the longitudinal slope of the flume was 0°.

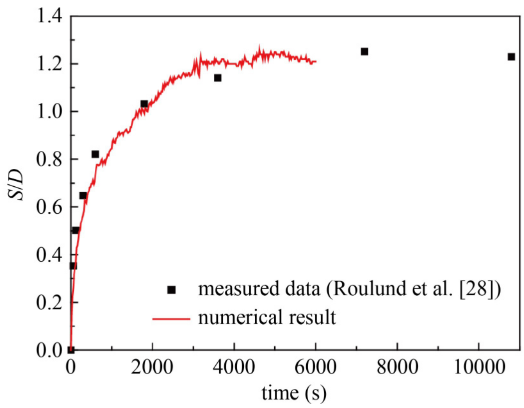

Fig. 4 Local scour depth development at the upstream edge of the pile.

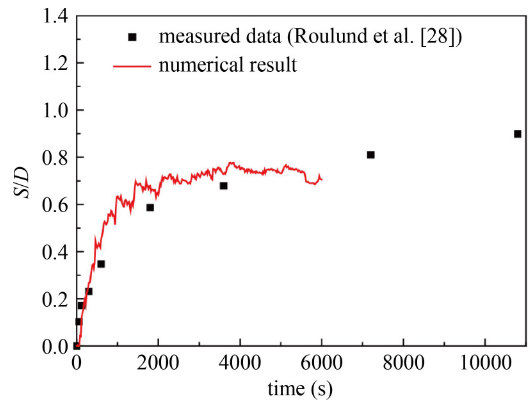

Fig. 5 Local scour depth development at the downstream edge of the pile.

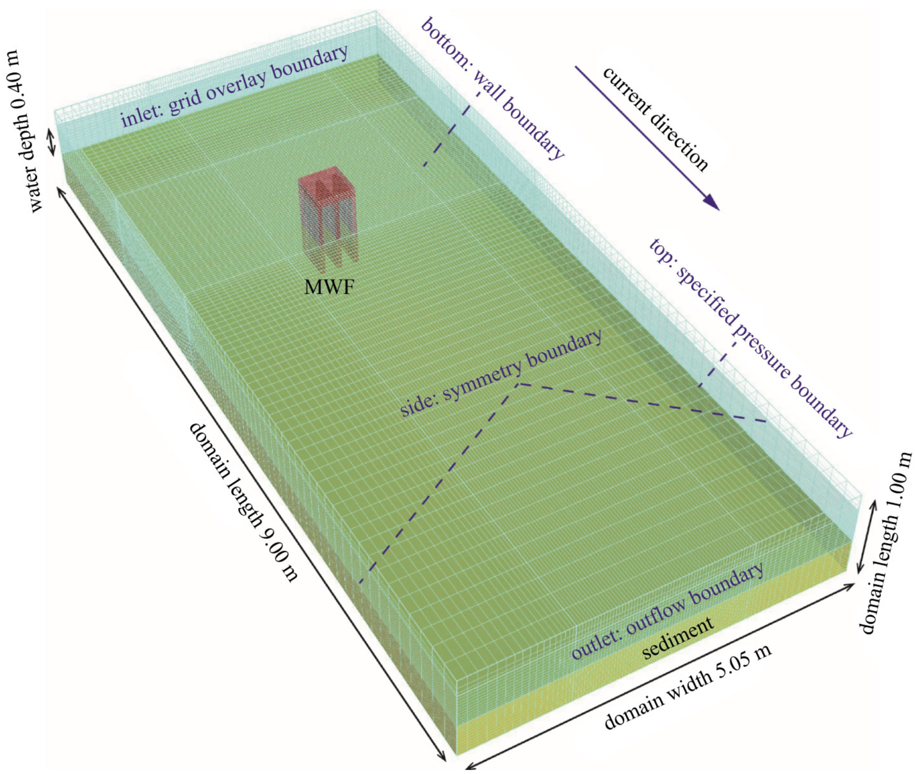

Fig. 6 Numerical model of MWF subjected to current-induced scour.

5 Results and discussion

5.1 Flow field analysis

Based on the simulation results, the flow field distribution and shape under unidirectional flow conditions are shown in Figs. 8 and 9. For convenience, the MWF with parallel wall arrangement at an inflow angle of 0° is abbreviated as "MWF-pr0," and the MWF with round wall arrangement is abbreviated as "MWF-rr0." Similarly, the MWF foundations at an inflow angle of 45° are abbreviated as "MWF-pr45" and "MWF-rr45," respectively.

Figure 8 shows a cross-sectional view of the single-column streamline in the central x-axis of the water flow for the four MWFs. For be seen, a relatively significant water-blocking effect arises when the water flow is close to the front of the foundation wall for all four MWFs. The closer to the wall, the smaller the longitudinal velocity of the water flow. Figure 9 shows the flow velocity distributions of the four MWFs. When the water flow reaches the front of the foundation wall, the water flow velocity at the front of MWF-pr0 drops to approximately 0.27 m/s (Fig. 9(a)) from 0.46 m/s (see Table 1), and those of MWF-pr45, MWF-rr0, and MWF-rr45 drop to

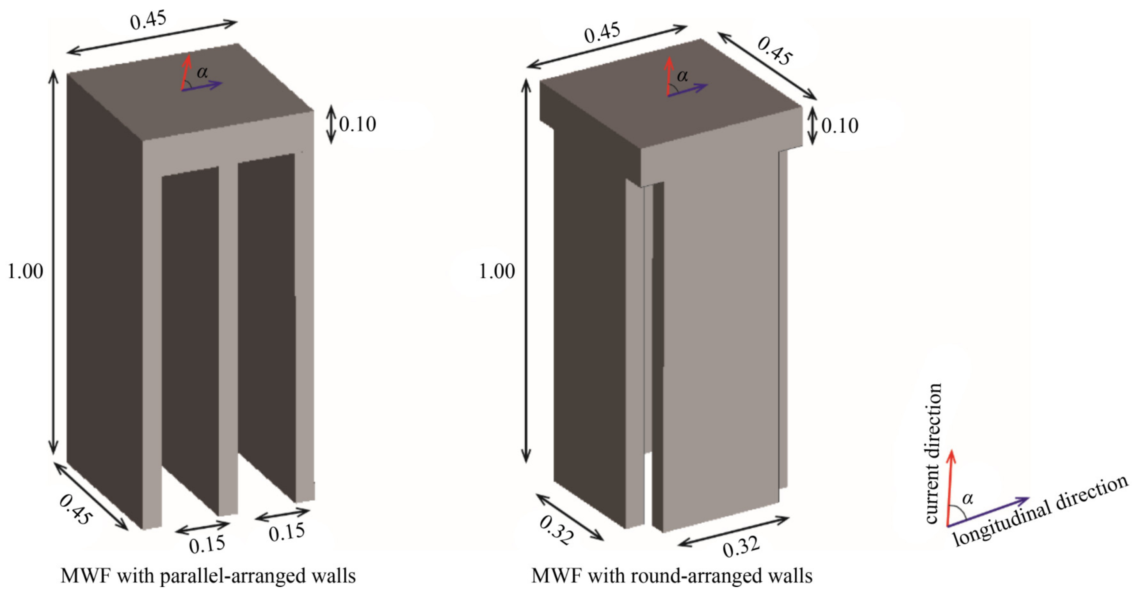

Fig. 7 MWF models adopted in the numerical analysis (unit: m).

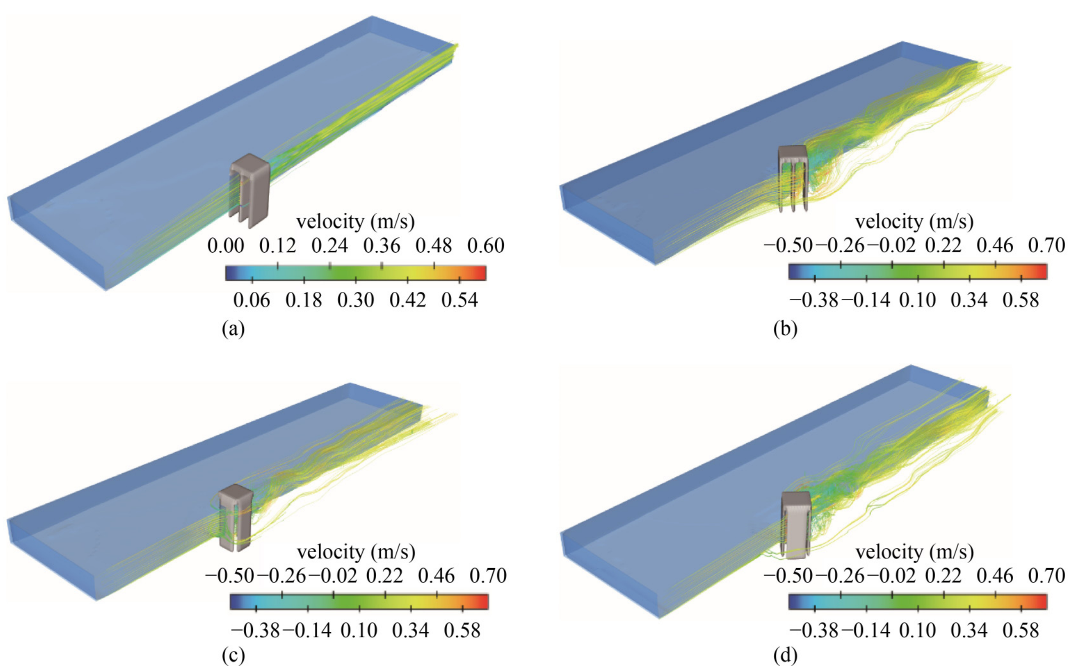

Fig. 8 Cross-sectional view of the single-column streamline: (a) MWF-pr0; (b) MWF-pr45; (c) MWF-rr0; (d) MWF-rr45.

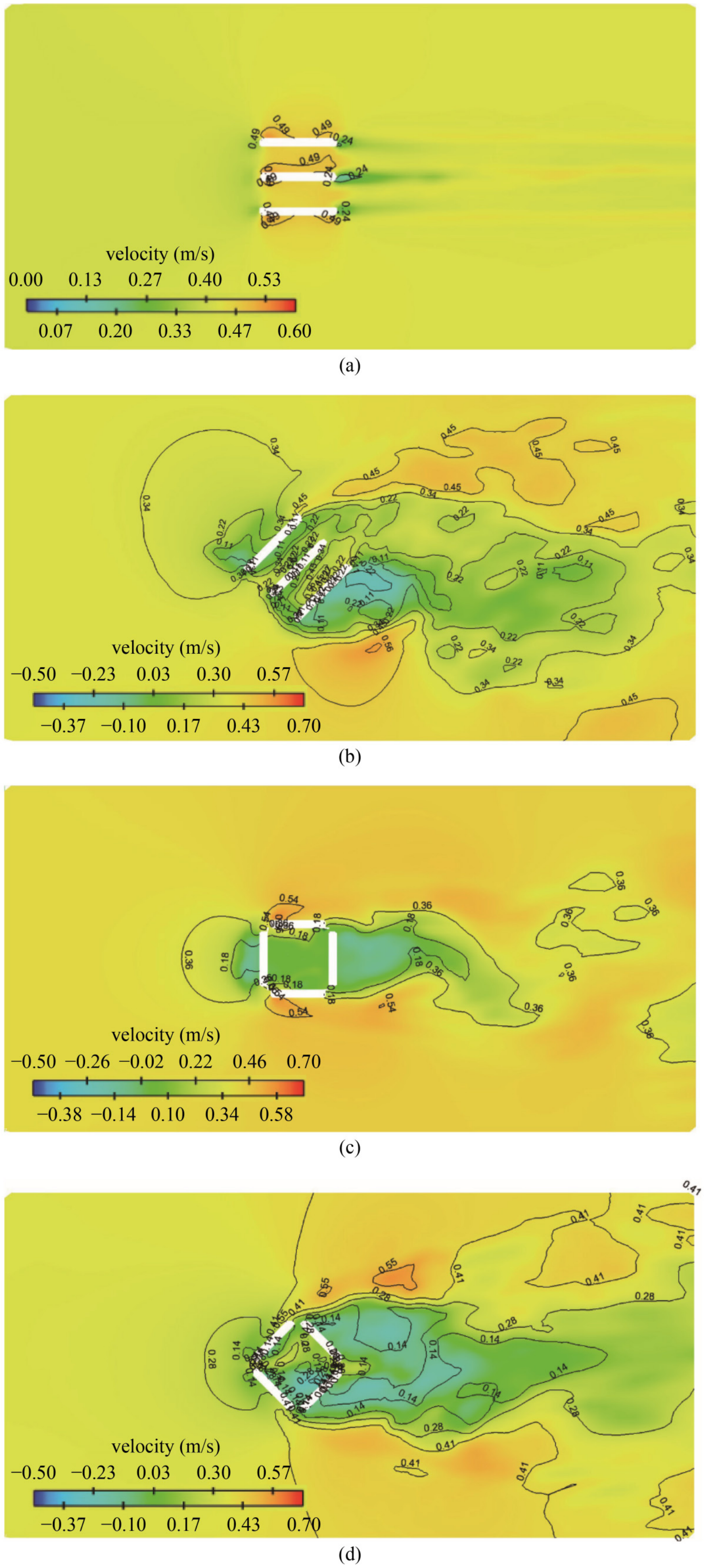

Fig. 9 Flow velocity field: (a) MWF-pr0; (b) MWF-pr45; (c) MWF-rr0; (d) MWF-rr45.

approximately 0.11 m/s (Fig. 9(b)), 0.18 m/s (Fig. 9(c)), and 0.14 m/s (Fig. 9(d)), respectively. In addition, Fig. 9 shows that the influence range of the water-blocking effect at the front wall of the four foundations is not the same and is greatly affected by the size of the contact area between the wall and the inflowing water. In summary, MWF-pr0 has the least blocking effect on the inflow water velocity, whereas MWF-pr45 has the most substantial effect.

As shown in Fig. 8, bypass flow is generated after the water flows through the front of the four MWFs. The flow velocity at the side of the foundation wall increases significantly because of the compression of the streamline, and the water flow accelerates significantly. As shown in Fig. 8, for the four foundations (particularly for the foundations other than MWF-pr0, which is arranged parallel to the 0° inflow angle), vortices and downward water flows are generated after the water flow bypasses the front of the foundation. The descending water flow gathers at the rear end of the wall, resulting in a negative flow velocity, thus forming a horseshoe vortex that can cause scouring of the bed sediment both upstream and downstream of the foundation.

The flow velocity distribution around the foundation in Fig. 9 reveals that, after the bypass flow occurs, the water flow velocity at the outer side of MWF-pr0, MWF-pr45, MWF-rr0, and MWF-rr45 increases to approximately 0.49, 0.56, 0.54, and 0.55 m/s, respectively. Owing to the separation of the fluid boundary layer on the side of the wall, a recirculation streamline zone appears after the separation point. Thus, a wake vortex forms, and the water flow produces a negative flow velocity. This phenomenon is evident for almost all MWFs, except MWF-pr0. As shown in Fig. 9, in the lower right part of the MWF-pr45 foundation, the rear end of the MWF-rr0 foundation and the middle and rear ends of the MWF-rr45 foundation have obvious vortices and a negative flow velocity of −0.5 m/s.

5.2 Local scour pit shape and development

To investigate the scour development and pit shape of the MWFs in each stage of the scouring process, the changes in the sediment elevation around the wall were analyzed from the time scale, and six moments were selected: 120, 300, 600, 1200, 2400, and 3600 s.

Figures 10 and 11 show the general and plan views of the scour development of MWF-pr0 at different times, respectively. As shown in Fig. 10, scour is not evident in the initial stage for MWF-pr0 arranged with parallel walls at an inflow angle of 0°. Over time, scour evolves around the wall and becomes more noticeable. Meanwhile, an apparent silting phenomenon can be observed at the rear end of the wall. Figure 11 shows that scouring mainly occurs around the two front sides of the wall at 120 s (Fig. 11(a)). The scouring depth is approximately −0.01 m, and a slight silting phenomenon appears near the front and rear ends of the wall. As the time increases, the scouring depth around the front side of the wall further develops, reaching −0.02 and −0.03 m at 300 and 600 s (Figs. 11(b) and 11(c)), respectively. The scouring depth and area on both sides of the inner wall are more significant than those on the outer wall. Moreover, the silting at the rear end of the wall reaches approximately 0.01 and 0.02 m at 300 and 600 s, respectively.

Figures 11(d)–11(f) show that the scour influencing range runs through the entire wall body and progressively spreads after the time exceeds 1200 s, and the maximum scour depth at 3600 s appears in the central bed area around the inner wall, which is approximately −0.06 m. Simultaneously, siltation continues to evolve at the rear end of the wall, and three relatively prominent silting bodies can be found at the rear end of the wall, with a maximum siltation height of approximately 0.03 m. When the scouring is relatively stable, the range of the scour pit is approximately 1.8 times the side length of the foundation cap (which is 0.45 m, as illustrated in Fig. 7) in the lateral direction and 1.7 times the length of the foundation cap in the vertical direction.

Figures 12 and 13 show the general and plan views of the scour development of MWF-pr45 (MWF with parallel-arranged walls at an inflow angle of 45°) at different times. As shown in Fig. 12, the scouring around MWF-pr0 is more evident at the initial stage compared with MWF-pr0, which is arranged with parallel walls at an inflow angle of 0°. Over time, the scouring evolves around the wall and radiates backward along the water flow on both sides of the inner and outer walls, finally forming a large scour pit. Meanwhile, an apparent silting phenomenon occurs at the rear end of the wall. Comparing Figs. 10 and 12 reveals that the scouring and siltation of MWF-pr45 are greater than those of MWF-pr0.

As shown in Figs. 13(a)–13(d), scouring is mainly generated around the two front sides of the wall from 120 to 1200 s. The scouring forms two irregular scouring pits, upper and lower, along the periphery of the wall, and the maximum scouring depth develops from −0.03 to −0.16 m. Meanwhile, a clear silting phenomenon appears near the rear end of the wall, increasing from 0.01 to 0.04 m. With further development over time after 2400 s, as shown in Figs. 13(e) and 13(f), the upper and lower irregular scouring pits along the wall periphery are connected, forming an asymmetric "heart-shaped" scouring pit centered on the body of MWF-pr45. The maximum scour depth is located near the front end of the wall. When the calculation is done at 3600 s, the maximum scouring depth reaches about −0.28 m, which is approximately 4.6 times that of MWF-pr0. The siltation body that eventually forms is located at the back of the scour pit, and the maximum siltation height reaches 0.06 m, which is approximately twice that of MWF-pr0. When the scour calculation is done, the range of the scour pit for MWF-pr45 is approximately 4.4 times the side length of the foundation cap in the lateral direction and 3.5 times the length of the foundation cap in the vertical direction. The scour pit area of MWF-pr45 is approximately five times that of MWF-pr0.

Figures 14 and 15 show the general and plan views of the scour development of MWF-rr0 (MWF with round-

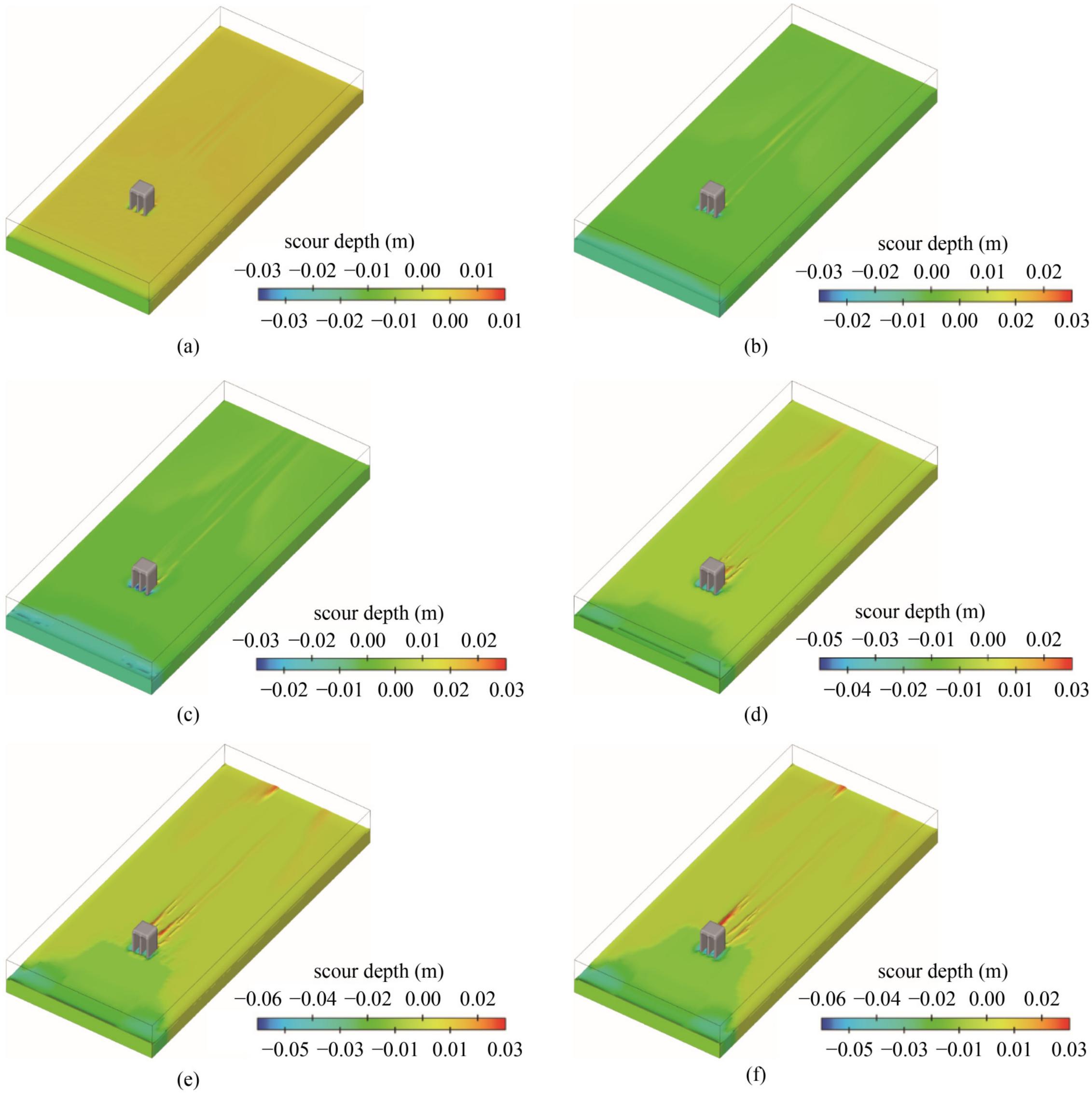

Fig. 10 Scour development for MWF-pr0: (a) 120 s; (b) 300 s; (c) 600 s; (d) 1200 s; (e) 2400 s; (f) 3600 s.

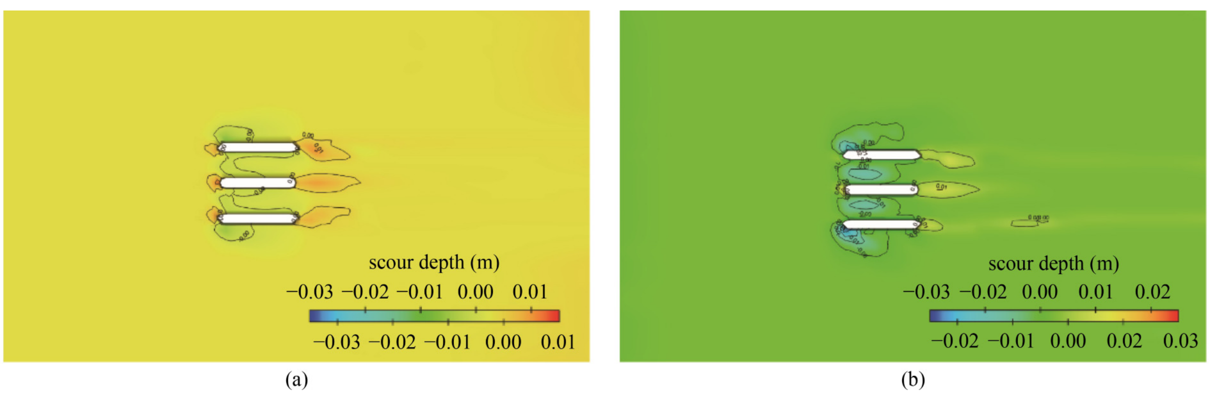

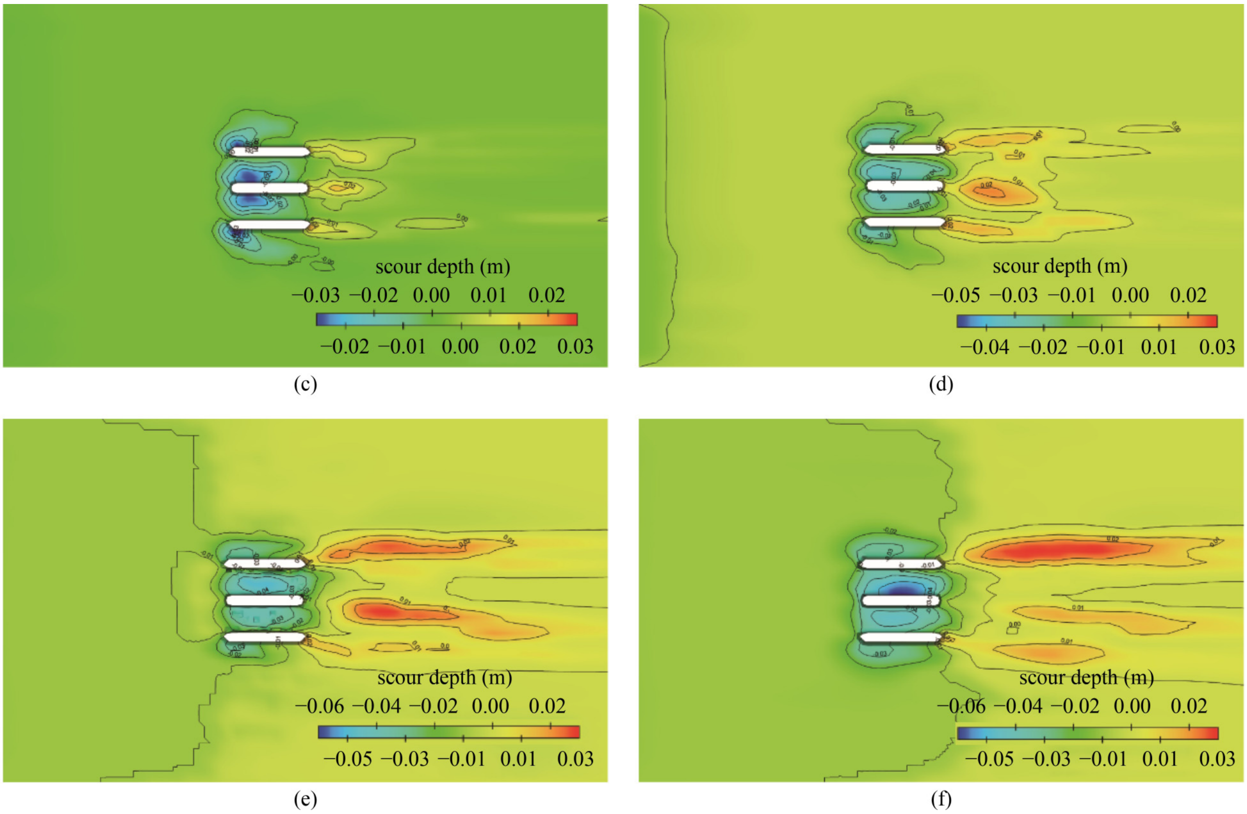

Fig. 11 Plan view of the scour pit for MWF-pr0 at different times: (a) 120 s; (b) 300 s; (c) 600 s; (d) 1200 s; (e) 2400 s; (f) 3600 s.

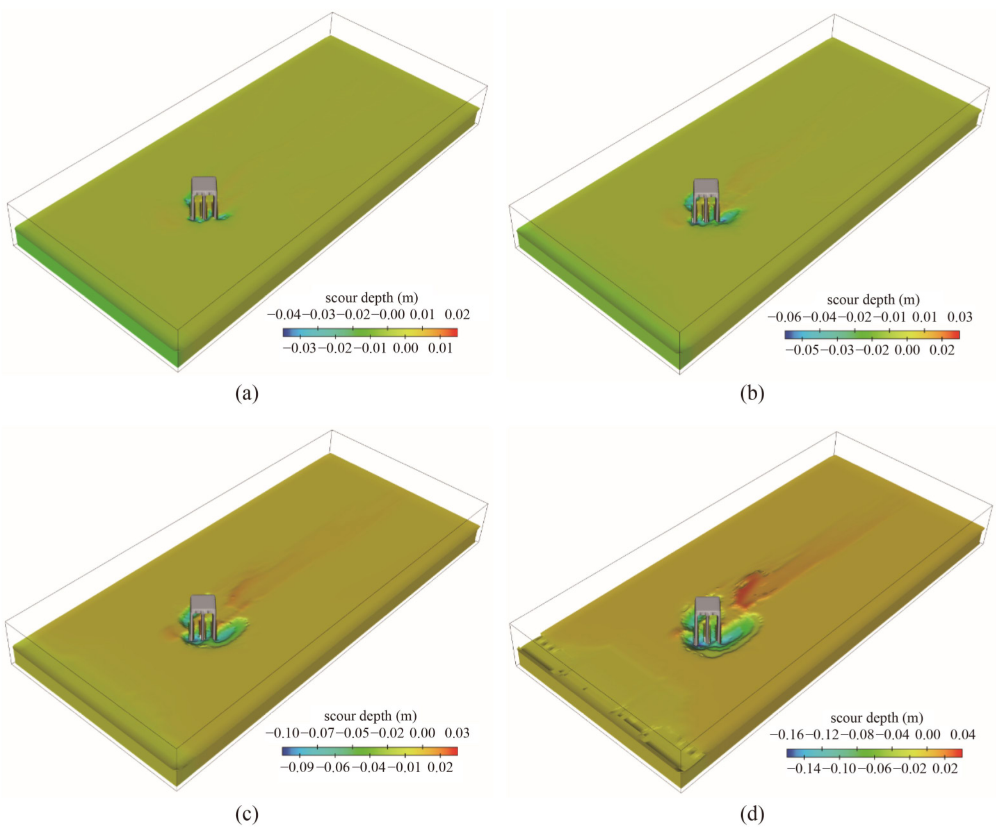

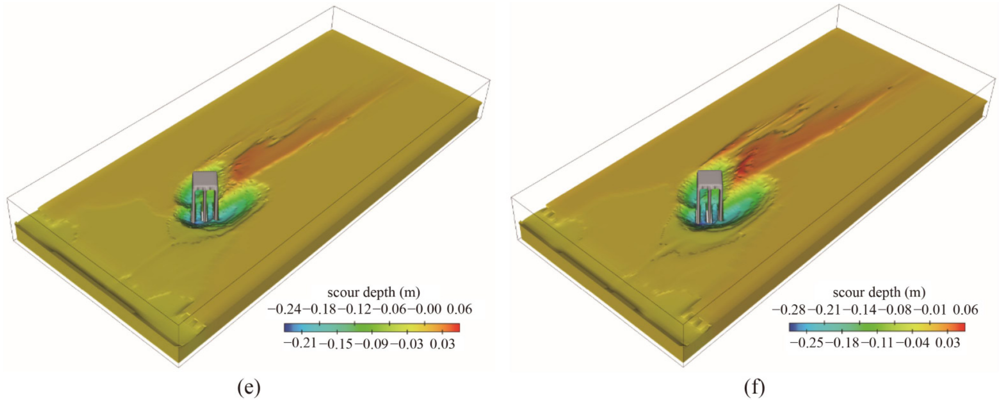

Fig. 12 Scour development for MWF-pr45: (a) 120 s; (b) 300 s; (c) 600 s; (d) 1200 s; (e) 2400 s; (f) 3600 s.

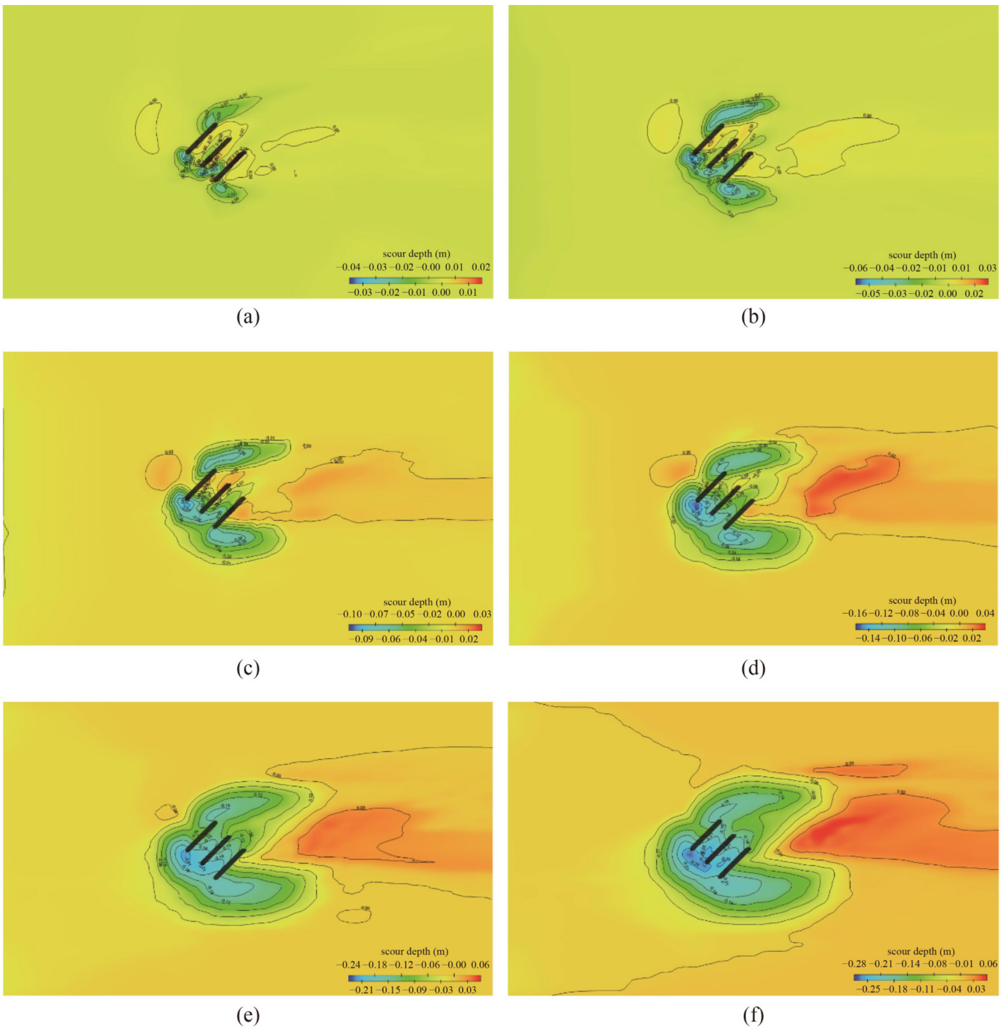

Fig. 13 Plan view of the scour pit for MWF-pr45 at different times: (a) 120 s; (b) 300 s; (c) 600 s; (d) 1200 s; (e) 2400 s; (f) 3600 s.

arranged walls at an inflow angle of 0°) at different times. As shown in Fig. 14, the scour around MWF-rr0 is more prominent at the initial stage compared with MWF-pr0, which is arranged with parallel walls at an inflow angle of 0°. Over time, the scouring evolves around the wall and radiates backward along the water flow on both sides of the inner and outer walls, finally forming a large scour pit. Meanwhile, a silting phenomenon can be clearly observed at the rear end of the wall. Comparing Figs. 10 and 14 reveals that the scouring and siltation of MWF-rr0 are more significant than those of MWF-pr0.

As shown in Figs. 15(a)–15(c), scouring mainly occurs

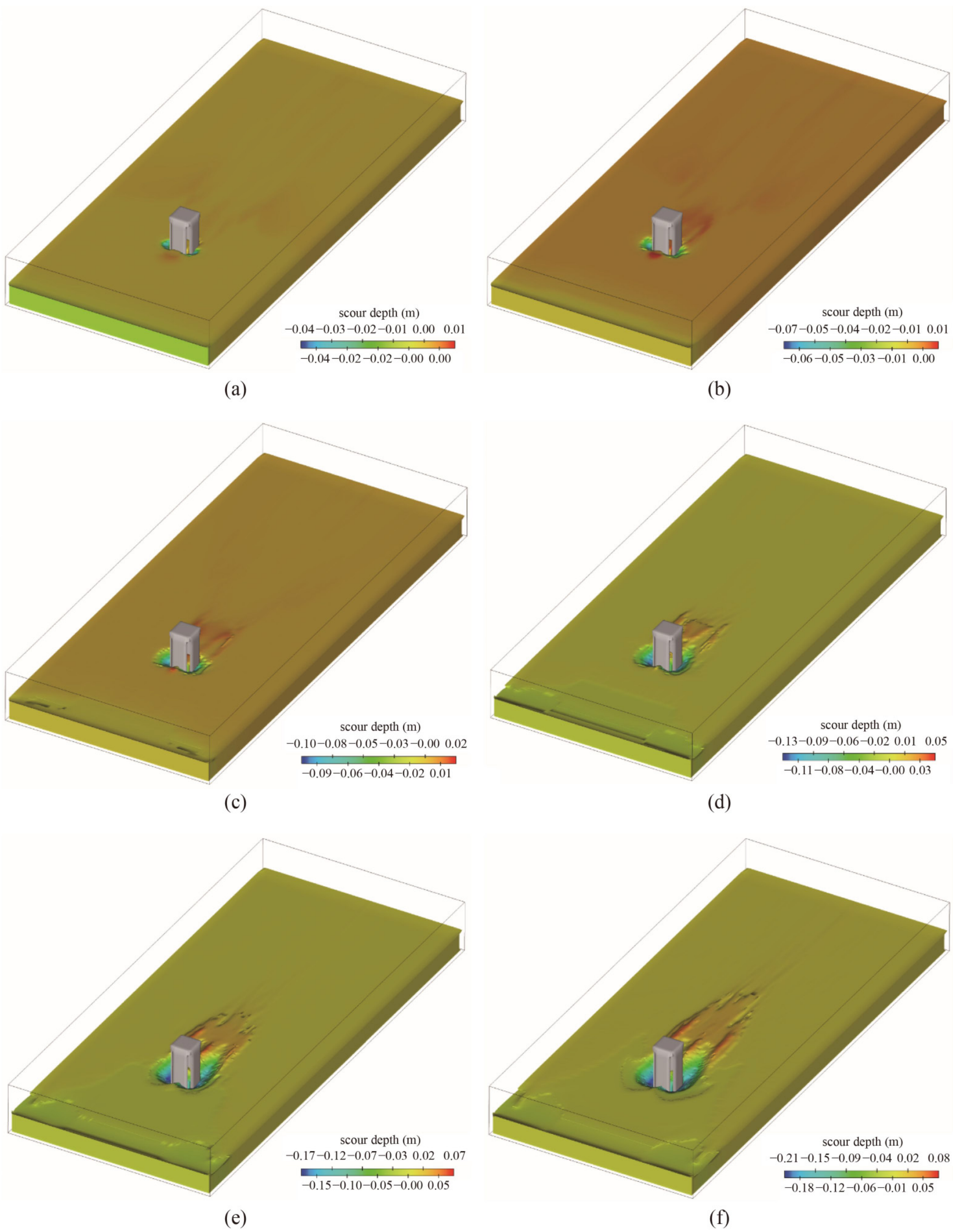

Fig. 14 Scour development for MWF-rr0: (a) 120 s; (b) 300 s; (c) 600 s; (d) 1200 s; (e) 2400 s; (f) 3600 s.

around the two front sides of the wall from 120 to 600 s for MWF-rr0, and it develops rapidly with time. The scouring forms two relatively regular and symmetric scouring pits, upper and lower, along the periphery of the wall, and the maximum scouring depth develops from –0.04 to –0.10 m. Meanwhile, an evident silting phenomenon appears inside the wall body and near the rear end of the wall, increasing from 0.01 to 0.02 m. With further development over time after 1200 s (Fig. 15(d)), the upper and lower scouring pits along the periphery of the wall are connected, forming a symmetric heart-shaped scouring pit centered on the body of MWF-rr0. The maximum scour depth is near the front end of the wall. When the calculation is done at 3600 s, the maximum scouring depth reaches approximately −0.21 m (Fig. 15(f)), which is approximately 3.5 times that of MWF-pr0. The siltation body that eventually forms is located at the back of the scour pit, and the maximum siltation height reaches 0.08 m, which is about 2.7 times that of MWF-pr0. When the scour calculation is done, the range of the scour pit for MWF-rr0 is approximately 4.0 times the side length of the foundation cap in the lateral direction and 3.5 times the length of the foundation cap in the vertical direction. The scour pit area of MWF-rr0 is approximately 4.6 times that of MWF-pr0.

Figures 16 and 17 show the general and plan views of

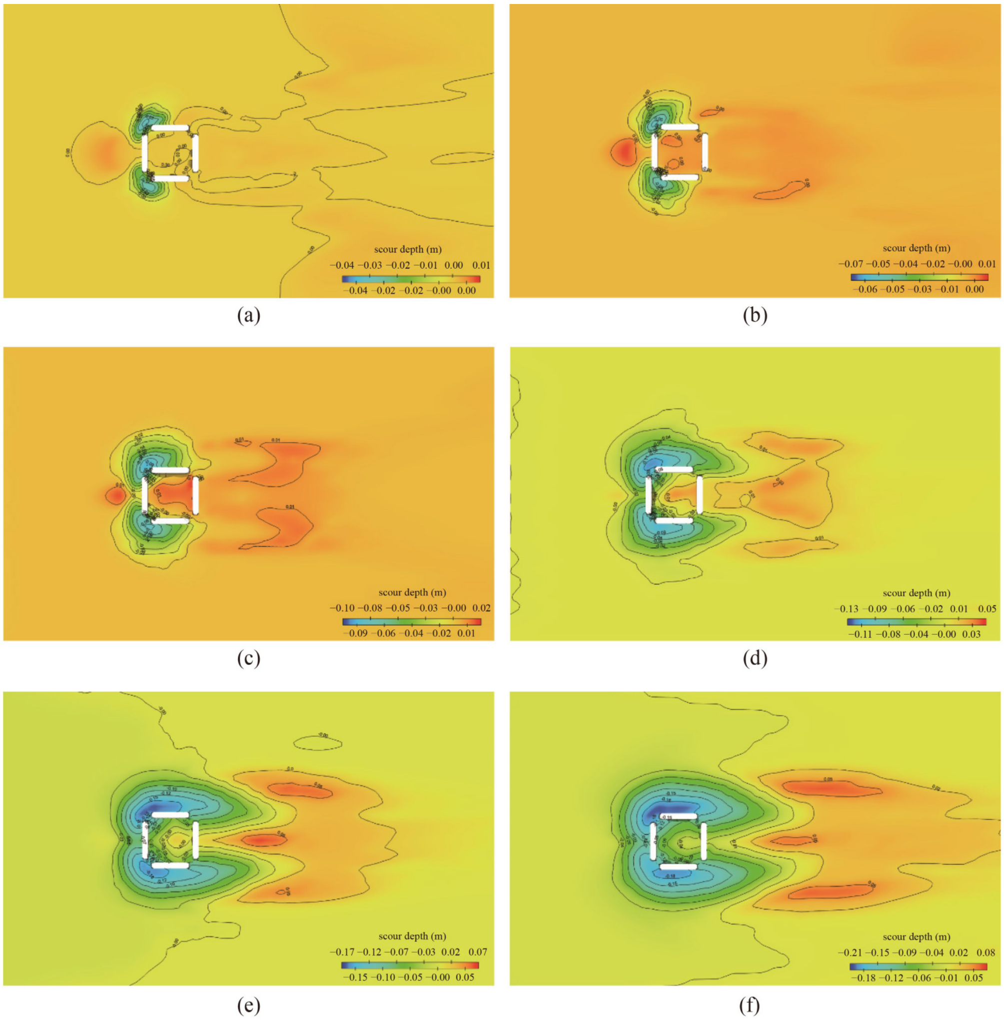

Fig. 15 Plan view of the scour pit for MWF-rr0 at different times: (a) 120 s; (b) 300 s; (c) 600 s; (d) 1200 s; (e) 2400 s; (f) 3600 s.

the scour development of MWF-rr45 (MWF with round-arranged walls at an inflow angle of 45°) at different times. As shown in Fig. 16, the scouring around MWF-rr0 is more significant at the initial stage than that around MWF-pr0 (Fig. 10). Over time, the scouring evolves around the wall and radiates backward along the water flow on both sides of the inner and outer walls, finally forming a large scour pit. Meanwhile, a silting phenomenon is clearly observed at the rear end of the wall. Comparing Figs. 10 and 16 reveals that the scouring and siltation of MWF-rr45 are more significant than those of MWF-pr0.

As shown in Figs. 17(a)–17(c), scouring is mainly generated inside the wall body and around the two front sides of the wall from 120 to 600 s for MWF-rr45, and it develops rapidly with time. The scouring forms three relatively regular and symmetric scouring pits (upper, middle, and lower) along the periphery of the wall, and the maximum scouring depth develops from −0.03 to −0.10 m. Meanwhile, an evident silting phenomenon appears inside the wall body and near the rear end of the wall, increasing from 0.02 to 0.03 m. With further development over time after 1200 s (Fig. 17(d)), the three scouring pits along the wall periphery are connected, forming a symmetric heart-shaped scouring pit centered on the body of MWF-rr45. The maximum scour depth is near the front end of the wall. Simultaneously, the siltation at the front end of the wall and inside gradually disappears owing to the action of water flow. When the calculation is done at 3600 s, the maximum scouring depth reaches approximately −0.25 m (Fig. 17(f)), which is about 4.2 times that of MWF-pr0. The siltation body that finally forms is located at the back of the scour pit, and the maximum siltation height reaches 0.08 m, which is approximately 2.7 times that of MWF-pr0. When the scour calculation is done, the range of the scour pit for MWF-rr45 is approximately 4.2 times the side length of the foundation cap in the lateral direction and 3.3 times the length of the foundation cap in the vertical direction. The scour pit area of MWF-rr45 is approximately 4.5 times that of MWF-pr0.

In general, the sizes and shapes of the scour pits of MWF-rr45 and MWF-rr0 are similar, and their maximum scour depths are also relatively close, which shows that

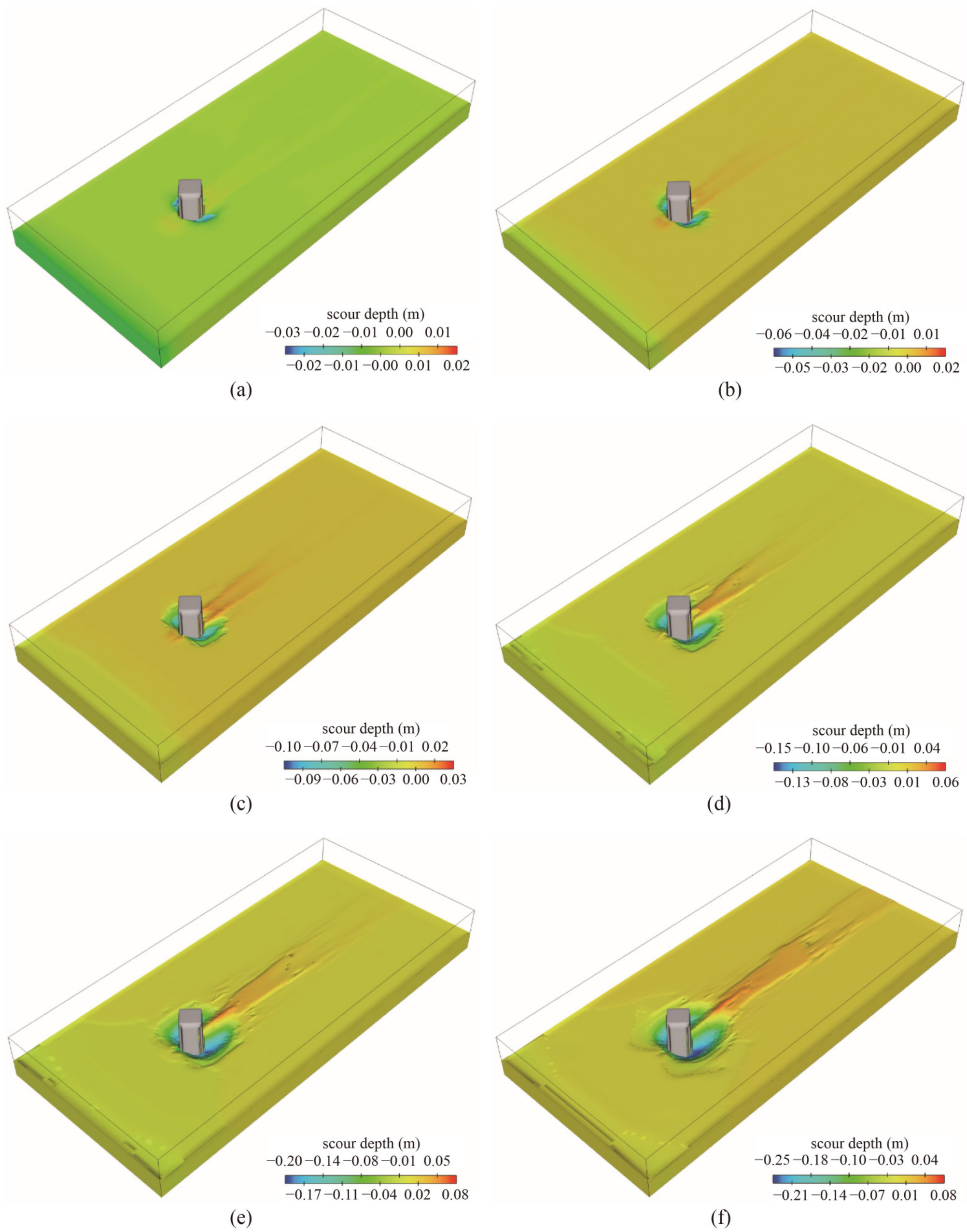

Fig. 16 Scour development for MWF-rr45: (a) 120 s; (b) 300 s; (c) 600 s; (d) 1200 s; (e) 2400 s; (f) 3600 s.

the inflow angle has little influence on the scouring effect of the MWF with round-arranged walls. As described above, for the MWF with an inflow angle of 0°, the size of the scour pit and the maximum scour depth of MWF-rr0 are much larger than those of MWF-pr0, demonstrating that the arrangement of the wall has a significant influence on the scour effect of the MWF. In other words, when the inflow angle is 0°, the MWF arranged in parallel has excellent scouring resistance, whereas the MWF arranged in a round configuration is vulnerable to scouring. In addition, for the MWF arranged in parallel, the scour pit range and maximum scour depth of MWF-pr45 are the largest among the four foundations, indicating that changing the inflow angle significantly impacts the scour characteristics of the MWF arranged in parallel.

5.3 Local scour depth

To analyze the generation and development process of the local scour pits around the four MWFs further, the local scour depths of the four foundations at different times along the central axis in the current direction and the direction perpendicular to the current are recorded and plotted in Figs. 18–21.

As shown in Fig. 18, for MWF-pr0 arranged in parallel and with an inflow angle of 0°, there is a specific siltation body near the front of the wall at the initial stage of

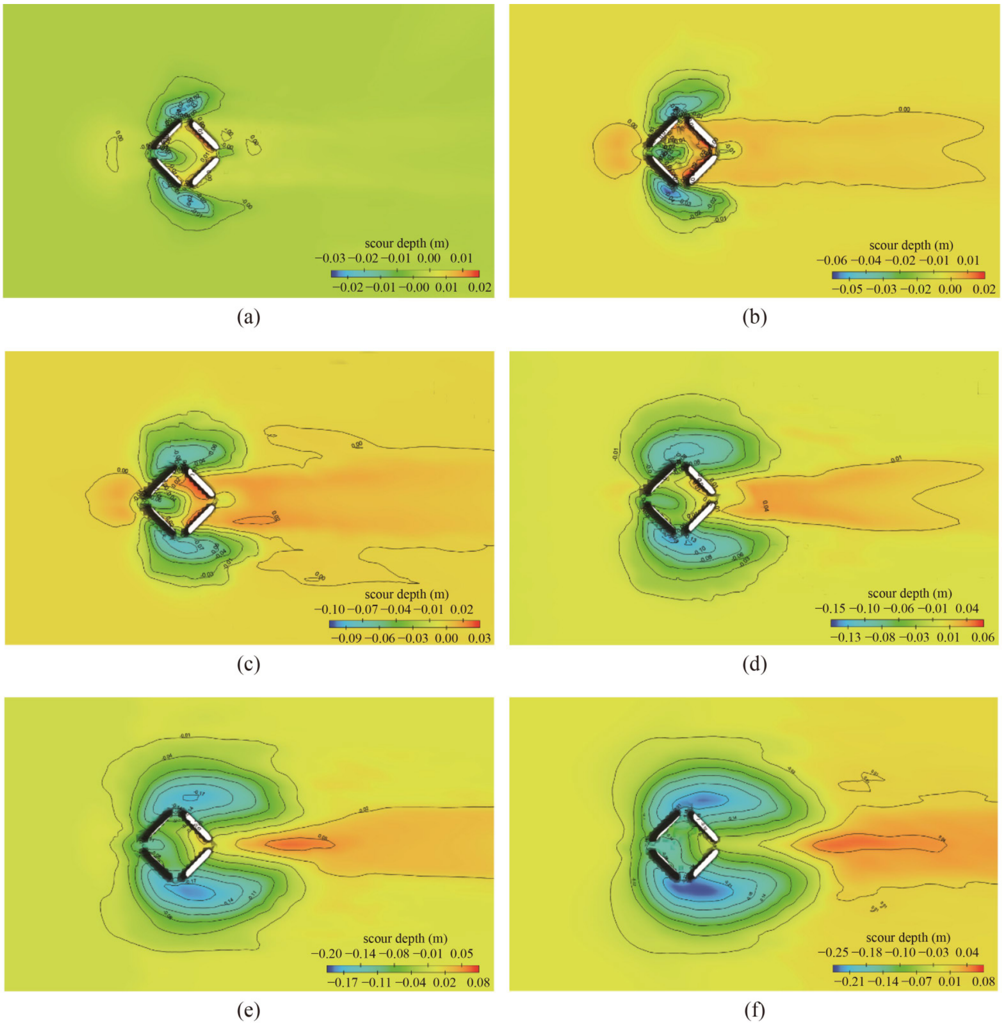

Fig. 17 Plan view of the scour pit for MWF-rr45 at different times: (a) 120 s; (b) 300 s; (c) 600 s; (d) 1200 s; (e) 2400 s; (f) 3600 s.

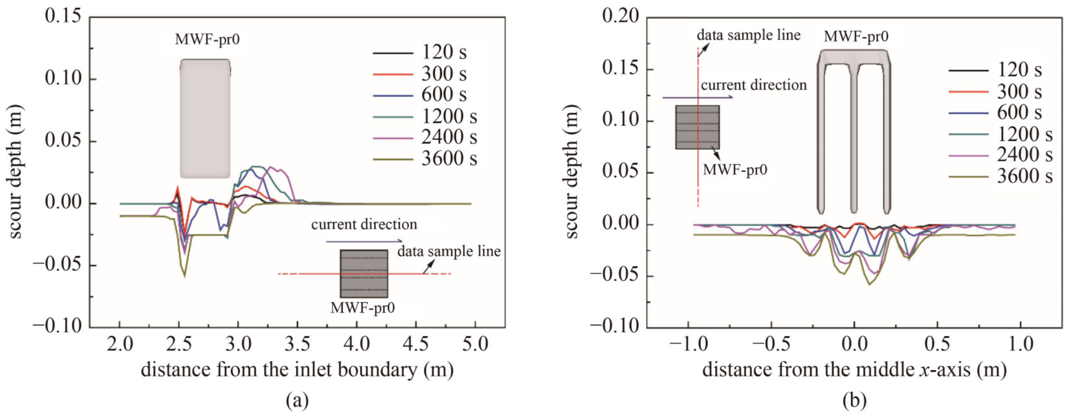

Fig. 18 Scour depth layout of MWF-pr0: (a) current direction and (b) direction perpendicular to the current.

scouring (Fig. 18(a)). Subsequently, scour occurs at the immediate front wall end, and a silt body appears at the rear end of the wall. With an increase in time, the scouring further develops, and the scouring depth at the front end of the wall deepens. Meanwhile, the front siltation body disappears, and the height of the siltation at the rear end of the wall increases further. The maximum central-axis scouring depth of the foundation in the current direction appears at the front wall end, which is approximately −0.06 m at 3600 s. In the direction perpendicular to the current (Fig. 18(b)), the scour phenomenon of MWF-pr0 increases with time. The scour

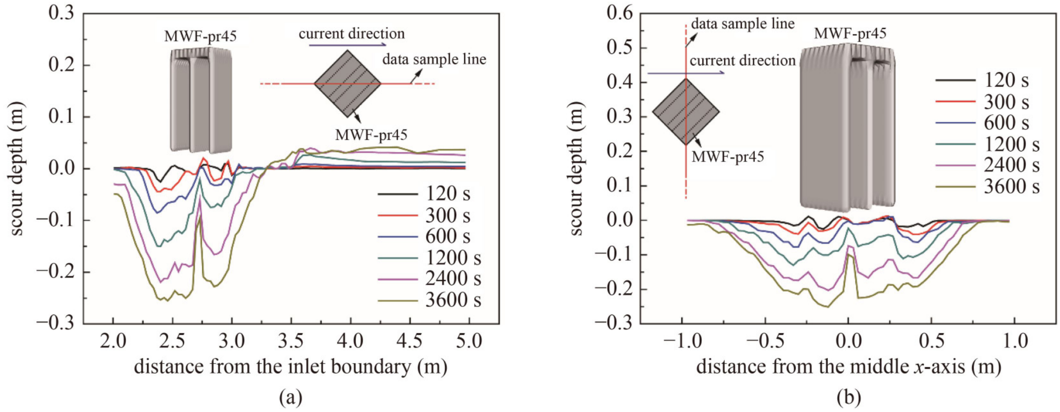

Fig. 19 Scour depth layout of MWF-pr45: (a) current direction and (b) direction perpendicular to the current.

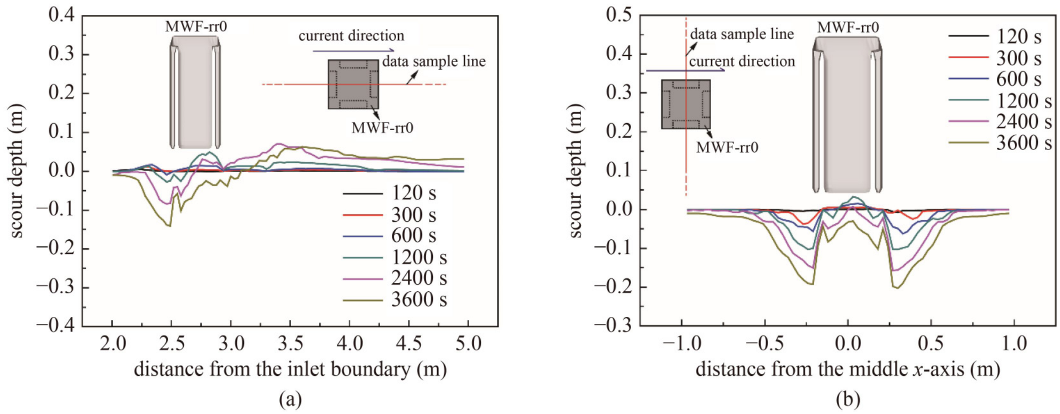

Fig. 20 Scour depth layout of MWF-rr0: (a) current direction and (b) direction perpendicular to the current.

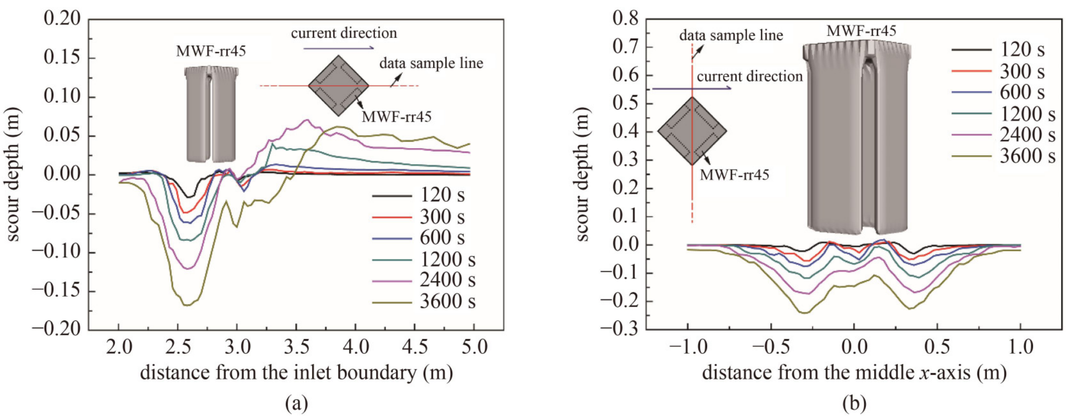

Fig. 21 Scour depth layout of MWF-rr45: (a) current direction and (b) direction perpendicular to the current.

mainly occurs around the wall profile, and the maximum scour depth is near the central wall (approximately −0.06 m). In addition, the silting phenomenon is not obvious in the direction perpendicular to the current for MWF-pr0.

As shown in Fig. 19, for MWF-pr45 arranged in parallel and with an inflow angle of 45°, the scour of the foundation deepens with time in the current direction (Fig. 19(a)), and the scour mainly occurs around the wall and inside. Siltation occurs at a position approximately 1.0 times the side length of the foundation at the rear end of the wall. The maximum central-axis scouring depth of the foundation in the current direction appears at the front wall end, which is approximately −0.25 m at 3600 s. In the direction perpendicular to the current (Fig. 19(b)), the scour phenomenon of MWF-pr45 increases with time. The scour mainly occurs around the wall profile and inside, and the maximum scour depth is near the front wall end, which is approximately −0.25 m. In addition, silting is not apparent in the direction perpendicular to the current for MWF-pr45.

Figure 20 shows that, for MWF-rr0 in a round configuration and with an inflow angle of 0°, the scouring of the foundation deepens with time in the current direction (Fig. 20(a)), and it mainly occurs around the wall and inside. Simultaneously, because the surrounding walls of MWF-rr0 are not closed, siltation occurs both inside the wall and near the rear end. With the development of scouring and the action of water flow, the internal siltation body gradually disappears, and the formed siltation body gradually moves backward. The maximum central-axis scouring depth of the foundation in the current direction appears at the front wall end, which is approximately −0.15 m at 3600 s. In the direction perpendicular to the current (Fig. 20(b)), the scour phenomenon of MWF-rr0 increases with time. The scour mainly occurs around the wall profile and inside, and the maximum scour depth appears near the two wall ends (approximately −0.20 m). In addition, the silting phenomenon is not evident in the direction perpendicular to the current for MWF-rr0.

As shown in Fig. 21, for MWF-rr45 arranged in a round configuration with an inflow angle of 45°, the scouring of the foundation deepens with time in the current direction (Fig. 21(a)), and it mainly occurs around the wall and inside. Simultaneously, because the surrounding walls of MWF-rr45 are not closed, siltation occurs both inside the wall and near the rear end. With the development of scouring and the action of water flow, the internal siltation body gradually disappears, and the formed siltation body gradually moves backward. The maximum central-axis scouring depth of the foundation in the current direction appears at the front wall end, which is approximately −0.17 m at 3600 s. In the direction perpendicular to the current (Fig. 21(b)), the scouring of MWF-rr45 increases with time. It mainly occurs around the wall profile and inside, and the maximum scour depth appears near the two wall ends (approximately −0.25 m). In addition, silting is not evident in the direction perpendicular to the current for MWF-rr45.

Figure 22 shows the comparison curves of the maximum scour depth of the four MWFs. In the calculation time range (3600 s), the maximum scour depth of MWF-pr0 is always smaller than the other three foundations, and its value stabilized at approximately −0.05 m after 2000 s. The maximum scour depths of MWF-rr45, MWF-rr0, and MWF-pr45 are relatively close in the initial stage. When the time exceeds 600 s, the maximum scour depth of MWF-pr45 becomes more significant than that of MWF-rr0 and MWF-rr45 and reaches approximately 0.28 m at 3600 s. The maximum scour depth of MWF-rr0 and MWF-rr45 is relatively close during the entire time. After the time exceeds 2000 s, the maximum scour depth of MWF-rr45 becomes slightly larger than that of MWF-rr0. At 3600 s, the maximum scour depth of MWF-rr0 and MWF-rr45 reach −0.21 and −0.25 m, respectively.

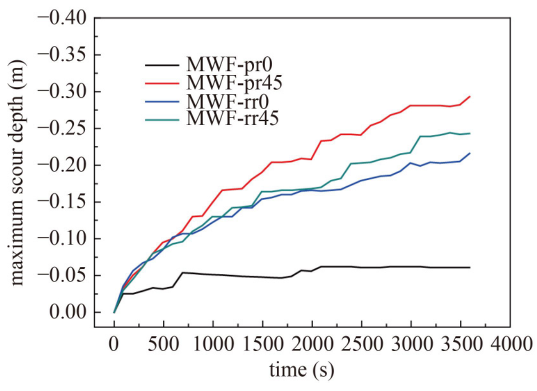

Fig. 22 Comparison of the maximum scour depths.

In general, the maximum scour depth of MWF-pr0 arranged in parallel with an inflow angle of 0° is much smaller than that of MWF-pr45 and the round-arranged MWFs, and its scouring reaches a steady-state quickly, showing excellent scouring resistance characteristics. Meanwhile, MWF-pr45, which is also arranged in parallel but with an inflow angle of 45°, has the largest maximum scour among the four foundations. For MWFs arranged in a round configuration, the maximum scour depth of MWF-rr45 with an inflow angle of 45° is slightly larger than that of MWF-rr0 with an inflow angle of 0°. At this point, one can infer that the maximum scour depth of MWFs with a 0° inflow angle is smaller than that of MWFs with a 45° inflow angle, regardless of the wall arrangement. For MWFs, in practical engineering design, MWFs arranged in parallel should be preferred, considering the need for scouring resistance. However, the scouring effect of the MWF arranged in parallel may be more significant than that of the round-arranged MWF in some cases when the inflow angle is not 0°, as described above. In addition, the round wall arrangement can improve the seismic performance of the MWFs by enhancing the horizontal stiffness. Therefore, a comparative analysis should be performed to consider comprehensively whether to adopt the form of a round wall arrangement when the inflow angle is not 0° or the inflow direction is changeable.

6 Conclusions

Scour is a primary trigger of bridges across rivers or seas. However, research concerning the scour mechanism of MWFs remains scarce, which can hinder their further application. In this study, the scouring effect caused by unidirectional flow in MWFs was investigated numerically using FLOW-3D. The following conclusions can be drawn.

1) The maximum scour depth of MWF-pr0 arranged in

parallel with an inflow angle of 0° is much smaller than that of MWF-pr45 and round-arranged MWFs. Its scouring reaches a steady-state quickly, showing excellent scouring resistance characteristics.

2) The sizes and shapes of the scour pits of MWF-rr45 and MWF-rr0 are similar, and their maximum scour depths are also relatively close, showing that the inflow angle has little influence on the scouring effect of the MWF with round-arranged walls.

3) When the inflow angle is 0°, an MWF arranged in parallel has excellent scouring resistance, whereas an MWF arranged in a round configuration is vulnerable to scouring. Meanwhile, the maximum scour depth of MWFs with a 0° inflow angle is smaller than that with a 45° inflow angle, regardless of the wall arrangement.

4) For the MWF arranged in parallel, the scour pit range and maximum scour depth of MWF-pr45 are the largest among the four foundations, indicating that changing the inflow angle significantly affects the scour characteristics of the MWF arranged in parallel.

5) For MWFs, in practical engineering design, MWFs arranged in parallel should be preferred, considering the need for scouring resistance. However, a comparative analysis should be performed to consider comprehensively whether to adopt the form of a round wall arrangement when the inflow angle is not 0° or the inflow direction is changeable.

Acknowledgements This research was funded by the National Nature Science Foundation of China (Grant No. 42007247), Nature Science Foundation of Sichuan Province (No. 2022NSFSC1151), Open Fund of Shock and Vibration of Engineering Materials and Structures Key Laboratory of Sichuan Province (No. 20kfgk08), Scientific and Technological Innovation Projects of Housing and Urban-rural Construction in Sichuan Province (No. SCJSKJ2022-09) as well as Selected Funding for Scientific and Technological Activities in Sichuan.

References

1. Wade K, Sugawara S, Wakababy N. Design and application of multi-wall foundation. Foundation Work, 1992, 2: 46−52 (in Japanese)
2. Wu J, El Naggar H M, Cheng Q, Wen H, Li Y, Zhang J. Iterative load transfer procedure for settlement evaluation of lattice-shaped diaphragm walls in multilayered soil. Computers and Geotechnics, 2020, 120: 103409
3. Ogasawara M, Kurokawa S. Design and construction of the underground multi-wall foundation. Journal of Civil Engineering, 1995, 36(4): 43−50 (in Japanese)
4. Sutherland A J. Reports on Ridge Failures. Road Research Unit Occasional Paper. Wellington: National Roads Board, 1986
5. Wardhana K, Hadipriono F C. Analysis of recent bridge failures in the United States. Journal of Performance of Constructed Facilities, 2003, 17(3): 144−150
6. Najafzadeh M, Barani G A. Comparison of group method of data handling based genetic programming and back propagation systems to predict scour depth around bridge piers. Scientia Iranica, 2011, 18(6): 1207−1213
7. Najafzadeh M. Neuro-fuzzy GMDH systems based evolutionary algorithms to predict scour pile groups in clear water conditions. Ocean Engineering, 2015, 99: 85−94
8. Najafzadeh M, Rezaie Balf M, Rashedi E. Prediction of maximum scour depth around piers with debris accumulation using EPR, MT, and GEP models. Journal of Hydroinformatics, 2016, 18(5): 867−884
9. Najafzadeh M, Oliveto G. More reliable predictions of clear-water scour depth at pile groups by robust artificial intelligence techniques while preserving physical consistency. Soft Computing, 2021, 25(7): 5723−5746
10. Najafzadeh M, Saberi-Movahed F, Sarkamaryan S. NF-GMDH-based self-organized systems to predict bridge pier scour depth under debris flow effects. Marine Georesources and Geotechnology, 2018, 36(5): 589−602
11. Homaei F, Najafzadeh M. A reliability-based probabilistic evaluation of the wave-induced scour depth around marine structure piles. Ocean Engineering, 2020, 196: 106818
12. Wang C, Yu X, Liang F. A review of bridge scour: Mechanism, estimation, monitoring and countermeasures. Natural Hazards, 2017, 87(3): 1881−1906
13. Liang F, Zhang H, Huang M. Extreme scour effects on the buckling of bridge piles considering the stress history of soft clay. Natural Hazards, 2015, 77(2): 1143−1159
14. Amini A, Parto A A. 3D numerical simulation of flow field around twin piles. Acta Geophysica, 2017, 65(6): 1243−1251
15. Amini A, Solaimani N. The effects of uniform and nonuniform pile spacing variations on local scour at pile groups. Marine Georesources and Geotechnology, 2018, 36(7): 861−866
16. Hosseini R, Fazloula R, Saneie M, Amini A. Bagged neural network for estimating the scour depth around pile groups. International Journal of River Basin Management, 2018, 16(4): 401−412
17. Khaledi V, Amini A, Bahrami J. Physical simulation of scour width and length variation around complex piers under clear water condition. Marine Georesources and Geotechnology, 2021, 39(9): 1107−1114
18. Yang Z. Large-eddy simulation: Past, present and the future. Chinese Journal of Aeronautics, 2015, 28(1): 11−24
19. Hirt C W, Sicilian J M. Porosity technique for the definition of obstacles in rectangular cell meshes. In: Proceedings-Fourth International Conference on Numerical Ship Hydrodynamics. Washington, D.C.: Office of Naval Research, 1985, 450−468
20. Othman Ahmed K, Amini A, Bahrami J, Kavianpour M R, Hawez D M. Numerical modeling of depth and location of scour at culvert outlets under unsteady flow conditions. Journal of Pipeline Systems Engineering and Practice, 2021, 12(4): 04021040
21. Moghadam M K, Amini A, Moghadam E K. Numerical study of energy dissipation and block barriers in stepped spillways. Journal of Hydroinformatics, 2021, 23(2): 284−297
22. Hu X, Guo P, Zhang Y, Mao J, Sun X, Sang T, Wang J. Buffeting noise characteristics and control of automobile side window. SAE International Journal of Vehicle Dynamics, Stability, and NVH,

2021, 5(1): 65−79
23. Soulsby R L. Bedload Transport. London: Thomas Telford Publications, 1997
24. Zhao M, Cheng L, Zang Z. Experimental and numerical investigation of local scour around a submerged vertical circular cylinder in steady currents. Coastal Engineering, 2010, 57(8): 709−721
25. Mastbergen D R, van Den Berg J H. Breaching in fine sands and the generation of sustained turbidity currents in submarine canyons. Sedimentology, 2003, 50(4): 625−637
26. Zhang Q, Zhou X L, Wang J H. Numerical investigation of local scour around three adjacent piles with different arrangements under current. Ocean Engineering, 2017, 142: 625−638
27. van Rijn L C. Sediment transport, Part I: Bed load transport. Journal of Hydraulic Engineering (New York, N.Y.), 1984, 110(10): 1431−1456
28. Roulund A, Sumer B M, Fredsøe J, Michelsen J. Numerical and experimental investigation of flow and scour around a circular pile. Journal of Fluid Mechanics, 2005, 534: 351−401
29. Yang Q, Yu P, Liu H. CFD modelling of local scour around Tri-USAF in sand with different arrangements under steady current. Ocean Engineering, 2021, 235: 109359
30. Deng X, He S, Cao Z. Numerical investigation of the local scour around a coconut tree root foundation under wave-current joint actions. Ocean Engineering, 2022, 245: 110563